The dam-break problem for viscous fluids in the high-capillary-number limit

C. ANCEY[1]†, S. COCHARD[2] AND N. ANDREINI[1]

[1]School of Architecture, Civil and Environmental Engineering, École Polytechnique Fédérale de Lausanne, 1015 Lausanne, Switzerland
[2]Department of Mathematics, University of British Columbia, Vancouver V6K 2A5, Canada

Experiments were undertaken to investigate dam-break flows where a finite volume of highly viscous fluid (glucose with viscosity $\mu \approx 350$ Pa s) maintained behind a lock gate was released into a horizontal or inclined flume. The resulting sequence of flow-depth profiles was tracked using a three-dimensional visualization system. In the low-Reynolds-number and high-capillary-number limits, analytical solutions can be obtained from the Navier–Stokes equations using lubrication theory and matched asymptotic expansions. At shallow slopes, similarity solutions can also be worked out. While the variation in the front position scaled with time as predicted by theory for both horizontal and sloping flumes, there was a systematic delay in the front position observed. Moreover, taking a closer look at the experimental flow-depth profiles shows that they were similar, but they noticeably deviated from the theoretical similarity form for horizontal planes. For sloping beds, the flow-depth profile is correctly predicted provided that different scalings are used at shallow and large slopes.

1. Introduction

The flow of a Newtonian fluid along a solid boundary has been extensively studied over the last 30 years owing to its importance and relevance to a wide range of applications in nature or industry. Much of the early work focused on buoyancy-driven flows at large Reynolds numbers as well as dense viscous gravity-driven currents (Simpson 1997; Huppert 2006). In the latter, a large body of literature has investigated contact-line instabilities arising from the competition between viscous and surface-tension effects, i.e. at low capillary numbers (Hocking 1990; Goodwin & Homsy 1991; Veretennikov, Indeikina & Chang 1998). The spread of a finite volume of viscous fluid along a horizontal surface or down a plane has also been extensively studied from the analytical point of view when surface tension and inertia are negligible compared to viscous forces. Attention was more specifically paid to the short- and long-time behaviour of fixed-volume and constant-inflow flows generated from a point or a line source (Smith 1969, 1973; Nakaya 1974; Huppert 1982*a*,*b*; Grundy 1983*a*; Gratton & Minotti 1990; Lister 1992). While most analytical results were worked out by seeking similarity solutions to the governing equations, a few results were also obtained using conformal-mapping techniques (Garabedian 1966; van Vroonhoven & Kuijpers 1990). Specific mathematical issues related to the

† Email address for correspondence: christophe.ancey@epfl.ch

existence of moving boundaries and how the solution to a particular initial value problem approaches the similarity form at infinite times have also been investigated (Ockendon 1978; Grundy & McLaughlin 1982; Grundy 1983*b*; Witelski & Bernoff 1998; Mathunjwa & Hogg 2006). In all the papers mentioned above, the governing equations were derived from the Navier–Stokes equations using lubrication theory; another approach taken by Hunt (1994) was to use flow-depth averaged equations of motion (i.e. the shallow-water equations) and solve them using singular perturbation techniques.

While buoyancy-driven turbulent flows have been carefully studied in the laboratory (Simpson 1997), there are few experimental investigations of time-dependent flows involving a Newtonian fluid over a solid boundary. Didden & Maxworthy (1982) and Maxworthy (1983) verified that for horizontal beds, inertial gravity currents eventually reach a viscous regime for which similarity theory provides a proper scaling of front evolution. A similar conclusion was drawn by Nsom, Debiane & Piau (2000) and Nsom (2002), who investigated the inertial-viscous transition for a glucose solution with viscosity $\mu = 12$ Pa s. Huppert (1982*a*,*b*) studied axisymmetric flows over both horizontal and sloping beds resulting from the collapse of small volumes (up to 1 litre) of silicon oils or glycerine with viscosities in the $0.1 - 1.5$ Pa s range. Although he worked with flows at fairly low capillary numbers (Ca as low as 10^{-2}), he observed that the front played no role in determining the shape and motion of the flow when the bottom was horizontal; in contrast, for sloping beds, the front quickly became unstable under surface-tension effects. Lister (1992) reported data related to point-source constant-flux and fixed-volume experiments carried out with glycerol or silicone (dynamic viscosities in the 0.1–35 Pa s range) and plane inclinations ranging from $2.5°$ to $17.5°$; he found good agreement between these data and the contact-line position predicted by similarity forms. Diez, Gratton & Gratton (1992) observed good agreement between similarity solutions and experimental results for converging axisymmetric flows on a horizontal bottom. Hunt (1994) presented experimental data obtained with plastic-bead suspensions placed on an inclined conveyor belt. Comparison with his asymptotic solutions to the shallow-water equations showed good agreement, but few details were provided. More recently, Takagi & Huppert (2007) investigated the effect of confining boundaries on front propagation. In all experimental results cited above, it is worth noting that the flow regime was characterized by low capillary numbers, which leads to the thinking that flows on sloping beds were affected to some degree by surface-tension effects; for most experimental settings, the flow Reynolds number Re was relatively large, with the low-Reynolds-number regime achieved at long times only. Moreover, attention was focused on how the front position scaled with time; there was no systematic comparison between experimental data and theory, in particular for the flow-depth profiles.

In this paper, we experimentally investigate the dam-break problem for a Newtonian fluid, where a fixed volume of fluid is suddenly unleashed from a reservoir and flows in a flume, which can be inclined or horizontal. We focus our attention on flow regimes in the large-capillary-number and low-Reynolds-number limit such that inertia and surface tension can be neglected in the analysis of flow motion. As far as we are aware, these experimental data are unique. In §2, we begin with a review of earlier theoretical work on thin viscous sheets. We consider the idealized two-dimensional problem of the instantaneous removal of a dam. The dam perpendicular to the slope initially retains a reservoir, as shown in figure 1. The fluid can then spread along a dry horizontal flume or flow down an inclined flume. For this setting, the governing equations are derived
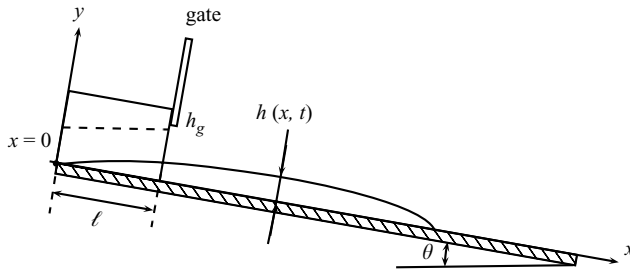
FIGURE 1. Sketch defining the flow configuration.

from the Navier–Stokes equations using lubrication theory, as shown by Mei (1966) and Buckmaster (1977). We then review and extend the results obtained by Huppert (1982a,b) and Lister (1992). Like these authors, we seek similarity solutions and use the method of matched asymptotic expansions to work out analytical solutions for determining the short- and long-time behaviour of the flow. Since this analysis holds for shallow slopes only, we then extend the theory to take slope effect into account (see §3). In §4, we present our experimental results. An innovative point is the measurement system, made up of a high-speed camera and micro-mirror projector, which makes it possible to accurately reconstruct the free surface of the flow at fairly high acquisition rates (up to 45 Hz). Finally, the experimental results are compared with analytical approximations of the Navier–Stokes equations, with emphasis given to front evolution and flow-depth profiles.

2. Diffusive–convective regime

2.1. *Notation and governing equation*

We consider an infinite plane tilted at an angle θ to the horizontal. We use a Cartesian coordinate system, where $\tilde{x}$ denotes the downstream coordinate measured from the top of the plane, while $\tilde{y}$ denotes the coordinate normal to the slope (see figure 1). Tilde variables are physical variables (the corresponding variables with no tilde are dimensionless). A rectangular box of length $\tilde{\ell}$, equipped with a gate perpendicular to the slope and placed at the plane inlet is partially filled with a volume $\tilde{V}$ of a Newtonian fluid with viscosity μ, surface tension γ and density ρ. The leftward end of this reservoir is chosen to be the origin of the x-axis. At time $\tilde{t} = 0$, the gate is suddenly opened and the fluid is released onto the plane. Initially the flow depth is denoted by

$$\tilde{h}_i(\tilde{x}) = \tilde{h}_g + (\tilde{x} - \tilde{\ell})\tan\theta, \tag{2.1}$$

with $\tilde{h}_g$ the gate aperture.

We are interested in determining the position x_f of the front and the flow-depth profile $h(x, t)$ with time t; h is the flow depth measured normal to the plane. We focus on shallow gravity-driven flows of highly viscous fluids on slopes, i.e. in the limit of high capillary number and low Reynolds and aspect-ratio numbers: $Ca = \mu U_*/\gamma \gg 1$, $\epsilon = H_*/L_* \ll 1$ and $Re = \rho U_* H_*/\mu \ll 1$, where H_* denotes the flow-depth scale, while U_* and L_* are the velocity and length scales, respectively. We also define the characteristic time $T_* = L_*/U_*$ and pressure scale $P_* = \rho g H_* \cos\theta$. To be consistent with volume conservation, we select the length and depth scales L_* and H_* such that $L_* H_* = \tilde{V}$, that is, $L_* = \sqrt{\tilde{V}/\epsilon}$ and $H_* = \sqrt{\epsilon \tilde{V}}$.

We introduce the dimensionless velocity components $(\tilde{u}, \tilde{v}) = (U_* u, \epsilon U_* v)$, pressure $\tilde{p} = P_* p$, coordinates $(\tilde{x}, \tilde{y}) = (L_* x, H_* y)$. The governing equations are given by the Navier–Stokes equations in a dimensionless form

$$\frac{\partial u}{\partial x} + \frac{\partial v}{\partial y} = 0, \tag{2.2}$$

$$\epsilon Re \frac{\mathrm{d}u}{\mathrm{d}t} = \phi \cos\theta \left(\tan\theta - \epsilon \frac{\partial p}{\partial x} \right) + \epsilon^2 \frac{\partial^2 u}{\partial x^2} + \frac{\partial^2 u}{\partial y^2}, \tag{2.3}$$

$$\epsilon^2 Re \frac{\mathrm{d}v}{\mathrm{d}t} = -\phi \cos\theta \left(1 + \frac{\partial p}{\partial y} \right) + \epsilon^3 \frac{\partial^2 v}{\partial x^2} + \epsilon \frac{\partial^2 v}{\partial y^2}, \tag{2.4}$$

with $\phi = \rho g H_*^2 / (\mu U_*)$ a dimensionless group. The mass and momentum balance equations are subject to the kinematic boundary conditions:

$$u = v = 0 \quad \text{for } y = 0 \tag{2.5}$$

at the bottom, while at the free surface, we have

$$v = \frac{\partial h}{\partial t} + u \frac{\partial h}{\partial x} \quad \text{for } y = h. \tag{2.6}$$

In addition, the dynamic condition at the free surface implies

$$(-p\phi \cos\theta \mathbf{1} + \boldsymbol{\sigma}) \cdot \mathbf{n} + \frac{\epsilon^2}{Ca} \frac{\mathbf{n}}{R} = 0 \quad \text{for } y = h, \tag{2.7}$$

with $\mathbf{n} = (-\epsilon \partial_x h, 1)$ a vector normal to the free surface, $R = (1 + \epsilon^2 (\partial_x h)^2)^{3/2} / \partial_{xx} h$ the curvature radius of the free surface and $\boldsymbol{\sigma}$ the extra-stress tensor. Mass conservation also implies that

$$V = \int_0^{x_f} h(x, t)\, \mathrm{d}x = \frac{1}{2} \ell (2 h_g - \kappa \ell) = 1, \tag{2.8}$$

with $\kappa = L_* \tan\theta / H_* = \tan\theta / \epsilon$. The flow depth vanishes at the front

$$h(x_f, t) = 0. \tag{2.9}$$

The initial value for h is

$$h(x, 0) = h_g + \kappa(x - \ell). \tag{2.10}$$

Hereafter we will address three limiting regimes: the *purely diffusive regime* occurs on horizontal bottoms ($\theta = 0$); motion is dictated by the balance between the streamwise gradient of the pressure and the cross-stream gradient of the shear stress, which implies that the proper velocity scale is $U_* = \rho g H_*^3 / (3\mu L_*)$ and $\phi = 3/\epsilon$. This regime has been extensively studied (Mei 1966; Nakaya 1974; Grundy & McLaughlin 1982; Huppert 1982b; Didden & Maxworthy 1982; Gratton & Minotti 1990) and for the sake of completeness we will briefly outline the results hereafter. For non-zero, but shallow slopes, the pressure/shear-stress balance is disturbed by the gravity forces. The resulting regime is referred to as the *diffusive–convective regime*. Since the aspect ratio ϵ cancels out in the dimensional equations, we have some freedom to select an appropriate value. Here we pose $\epsilon = \tan\theta$ and $\phi = 3/\sin\theta$ such that the streamwise gravitational component, the streamwise gradient of the pressure and the cross-stream gradient of the shear stress are of the same order; the corresponding velocity scale is then $U_* = \rho g H_*^2 \sin\theta / (3\mu)$, that is, the mean velocity of a viscous sheet in a steady uniform regime. For larger slopes, this scaling no longer holds: motion is then governed by the balance between the gravity force and the cross-stream gradient

of the shear stress except for the tip region, where the strong curvature of the free surface gives strength to the pressure gradient. Here this regime is called the *slope-dominated regime*. In § 3, we will show using matched asymptotic expansions that ϵ scales as $\tan^2 \theta$. The velocity scale and the dimensionless group ϕ are the same as for the diffusive–convective regime; we will show that the slope-dominated and diffusive–convective regimes are physically very similar in spite of the differences in the aspect-ratio number ϵ.

2.2. *Purely diffusive and diffusive–convective regimes*

Keeping Re order one, taking the limit $Ca \to \infty$ and removing terms of order ϵ or higher in the governing equations (2.2)–(2.4), we transform the Navier–Stokes equations to obtain the following set of equations, where inertia and surface tension are negligible:

$$\frac{\partial u}{\partial x} + \frac{\partial v}{\partial y} = 0, \tag{2.11}$$

$$3\left(1 - \frac{\partial p}{\partial x}\right) + \frac{\partial^2 u}{\partial y^2} = 0, \tag{2.12}$$

$$1 + \frac{\partial p}{\partial y} = 0, \tag{2.13}$$

with the following boundary conditions at the free surface: $\partial_y u = 0$, $v = \partial_t h + u \partial_x h$ and $p = 0$. At the bottom, the no-slip condition holds: $u = 0$. Integrating the mass balance equation (2.11) yields the governing equation for h

$$\frac{\partial h}{\partial t} + \frac{\partial h \bar{u}}{\partial x} = 0,$$

with $\bar{u}$ the flow-depth averaged velocity given by integrating (2.12) twice: $\bar{u} = h^2(\partial_x p - 1)$. The pressure is obtained by integrating (2.13): $p = h - x$. We end up with a nonlinear diffusion–convection equation that governs the flow-depth variation with time

$$\frac{\partial h}{\partial t} + \frac{\partial h^3}{\partial x} = \frac{\partial}{\partial x}\left(h^3 \frac{\partial h}{\partial x}\right). \tag{2.14}$$

In this equation, the second term on the left-hand side represents convection of h at a velocity $3h^2$, while the third term represents nonlinear diffusion of the flow depth, with a diffusion coefficient equal to h^3. When the channel slope is zero, the convection term $\partial_x h^3$ must be removed from the governing equation (2.14) and the governing equation is then the nonlinear diffusion equation

$$\frac{\partial h}{\partial t} = \frac{\partial}{\partial x}\left(h^3 \frac{\partial h}{\partial x}\right). \tag{2.15}$$

There is no similarity solution to (2.14), but such solutions exist at early or late times when diffusion or convection, respectively, predominates. Without losing generality, we can seek solutions in the form

$$h(x, t) = t^{-n} H(\xi, t), \tag{2.16}$$

with $\xi = x/t^n$ and $n > 0$. Substituting form (2.16) into (2.8) yields

$$-3H^2\left(\frac{\partial H}{\partial \xi}\right)^2 t^{1-5n} - H^3 \frac{\partial^2 H}{\partial \xi^2} t^{1-5n} + 3H^2 \frac{\partial H}{\partial \xi} t^{1-3n} = Hn + n\xi \frac{\partial H}{\partial \xi} - \frac{\partial H}{\partial t} t. \tag{2.17}$$

The first two terms on the left-hand side represent diffusion, while the third term arises from convection; the right-hand side represents the flow-depth variations with time. At long times, $t^{1-3n} \gg t^{1-5n}$, implying that convection is the prevailing mechanism, while at short times, $t^{1-3n} \ll t^{1-5n}$ implies predominance of diffusion. For these respective contributions to be of finite order, we pose $n = 1/5$ when seeking similarity solutions on short times and $n = 1/3$ for long times.

2.3. *Short-time similarity solutions*

To find similarity solutions, we pose $n = 1/5$ and $H(\xi, t) = \Psi_0 + t^{\lambda_1}\Psi_1(\xi) + \cdots + t^{\lambda_i}\Psi_i(\xi) + \cdots$, with $\lambda_i > 0$ and Ψ_i functions of ξ. In the limit of $t \to 0$ and with $\xi = O(1)$, (2.17) reduces to

$$\Psi_0 + \xi\Psi_0' + 15(\Psi_0\Psi_0')^2 + 5\Psi_0^3\Psi_0'' = 0,$$

whose integration provides

$$\xi\Psi_0 + 5\Psi_0^3\Psi_0' = c,$$

with c a constant of integration. Since at the front ξ_f, the flow depth vanishes, we obtain $c = 0$. A new integration leads to the solution

$$h(x, t) = t^{-1/5}\left(\frac{3}{10}\left(\xi_f^2 - \xi^2\right)\right)^{1/3}. \tag{2.18}$$

A mass balance equation (2.8) allows us to determine ξ_f:

$$\xi_f = V^{3/5}\left(\frac{\sqrt[3]{3/10}\sqrt{\pi}\Gamma(1/3)}{5\Gamma(5/6)}\right)^{-3/5} \approx 1.411 V^{3/5}, \tag{2.19}$$

where Γ denotes the gamma function. We retrieve the solution worked out notably by Nakaya (1974) and Huppert (1982*b*). Equation (2.18) arises also in a number of nonlinear diffusion processes, where it is referred to as the Barrenblatt–Pattle solution.

2.4. *Long-time similarity solutions*

We now pose $n = 1/3$, $H(\xi, t) = H_0 + t^{\nu_1}H_1(\xi) + \cdots + t^{\nu_i}H_i(\xi) + \cdots$ with $\nu_i > 0$ and H_i functions of ξ. As $t \to \infty$ while $\xi = O(1)$, (2.17) becomes

$$3H_0^2\frac{\partial H_0}{\partial \xi} - H_0 n - n\xi\frac{\partial H_0}{\partial \xi} = 0.$$

whose integration yields

$$H_0^3 = \tfrac{1}{3}\xi H_0 + c,$$

with c a constant of integration. Here we cannot apply the boundary condition $H_0(\xi_f) = 0$, which may mean that a boundary layer arises in the close vicinity of the front. H_0 is then the outer solution. We set $H_0 = 0$ at $\xi = 0$, which imposes $c = 0$. We finally find

$$H_0(\xi) = \sqrt{\frac{\xi}{3}}. \tag{2.20}$$

The front position ξ_f is still determined using mass balance conservation (2.8):

$$\xi_f = \left(\tfrac{3\sqrt{3}}{2}V\right)^{2/3}, \tag{2.21}$$

consistently with earlier results obtained by Huppert (1982*a*) and Lister (1992). A boundary layer occurs at the front because it is no longer possible to neglect the

curvature effect and diffusive terms in the governing equation (2.17). The following variable change is made to magnify what is occurring within this boundary layer:

$$\xi = \xi_f - \eta t^\sigma,$$

with $\sigma < 0$ a constant to be determined such that $\eta = t^{-\sigma}(\xi_f - \xi) = O(1)$. With this variable change, (2.17) becomes

$$\left(-3H^2 + \frac{1}{3}\xi_f\right)\frac{\partial H}{\partial \eta}t^{-\sigma} + \frac{\partial H}{\partial t}t - \frac{H}{3} - \frac{\eta}{3}\frac{\partial H}{\partial \eta} - \eta\sigma\frac{\partial H}{\partial \eta}$$
$$= \left[3H^2\left(\frac{\partial H}{\partial \eta}\right)^2 + H^3\frac{\partial^2 H}{\partial \eta^2}\right]t^{-2/3-2\sigma}.$$

Since $\sigma < 0$, the right-hand side must counterbalance the first two terms on the left-hand side, which imposes $\sigma = -2/3$. We then use the expansion for the inner similarity solution:

$$H(\xi, t) = K_0 + t^{\chi_1}K_1(\xi) + \cdots,$$

with $\chi_i < 0$ and K_i functions of ξ alone. The equation governing K_0 is

$$-3K_0^2\frac{\mathrm{d}K_0}{\mathrm{d}\eta} + \frac{1}{3}\xi_f\frac{\mathrm{d}K_0}{\mathrm{d}\eta} - 3K_0^2\left(\frac{\mathrm{d}K_0}{\mathrm{d}\eta}\right)^2 - K_0^3\frac{\mathrm{d}^2K_0}{\mathrm{d}\eta^2} = 0, \tag{2.22}$$

with the following conditions:

$$K_0(\eta_f) = 0, \tag{2.23}$$

$$\lim_{\eta\to\infty}K_0 = \lim_{\xi\to\xi_f}H_0(\xi) = \sqrt{\frac{\xi_f}{3}} = K_\infty, \tag{2.24}$$

η_f being the value of η at the front. Integrating (2.22) yields

$$\eta - \eta_f = \eta_s(K_0) = \int_0^{K_0}\frac{\mathrm{d}k}{(1/3)(\xi_f/k^2) - 1} = K_\infty\tanh^{-1}\left(\frac{K_0}{K_\infty}\right) - K_0. \tag{2.25}$$

Equation (2.25) is an implicit equation for the flow depth $K_0(\eta)$ within the boundary layer. To determine η_f, we assume that within the boundary layer, mass is merely redistributed with no creation or loss:

$$|\eta_f|K_e - K_\infty\int_0^{K_e}\eta_s(K)\mathrm{d}K = K_\infty\int_{K_e}^{K_\infty}\eta_s(K)\mathrm{d}K - (K_\infty - K_e)|\eta_f|,$$

where K_e is the K value for which $\eta_s(K_e) = 0$. After rearrangement, we find

$$K_\infty|\eta_f| = K_\infty^2\left(\log 2 - \tfrac{1}{2}\right),$$

which gives

$$\eta_f = -\left(\log 2 - \tfrac{1}{2}\right)K_\infty \approx -0.193K_\infty < 0.$$

The thickness of the boundary layer accounts for approximately 20% of the front depth given by the outer solution.

2.5. *Summary and remarks*

To summarize the computations, we have found that the front position is given by

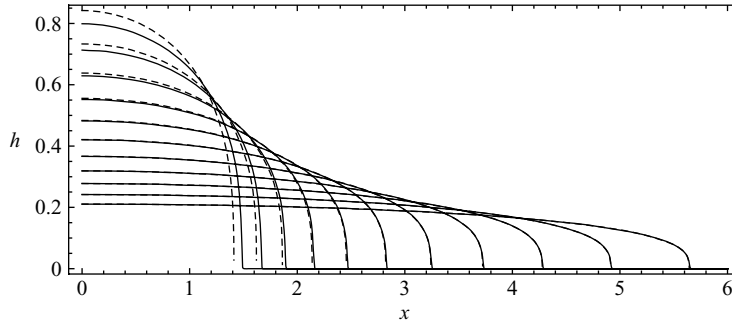$$x_f = \xi_f t^{1/3} + \left(\log 2 - \tfrac{1}{2}\right)\sqrt{\frac{\xi_f}{3}}t^{-1/3}, \tag{2.26}$$

FIGURE 2. Flow-depth profiles provided by the numerical solutions (solid line) of the nonlinear diffusion equation (2.15) for $\theta = 0°$ and at times $t = 1, 2, 4, 8, 16, 32, 64, 128, 256, 512$ and 1024. The similarity solutions (2.18) are also reported (dashed line).

with ξ_f given by (2.21). The flow depth is the composite of the inner and outer solutions

$$h(x,t) = t^{-1/3} \left(\sqrt{\frac{1}{3} \frac{x}{t^{1/3}} + K_0 \left((\xi_f - xt^{1/3}) t^{2/3} \right)} - \sqrt{\frac{\xi_f}{3}} \right). \qquad (2.27)$$

Huppert (1982a) and Lister (1992) derived the same outer solution (2.20). In their derivation, the diffusive term arising from the flow-depth gradient in the mean velocity is neglected†.

Apart from analytical approximations (e.g. the similarity solutions worked out above), there is no full analytical solution to the initial boundary value problem (2.2)–(2.10), which must be then solved numerically. For this purpose we used the *pdepe* routine provided in Matlab to solve parabolic differential equations in one space variable.

Figure 2 shows flow-depth profiles at different times ranging from 1 to 1024 when the flume inclination is set to zero. We also reported the similarity solutions (2.18) corresponding to pure diffusion. As documented in earlier papers (Mathunjwa & Hogg 2006), the solution of the initial value problem tends rather quickly towards the similarity solutions. Even at short times, there is not much difference between the front position computed numerically and that given by (2.19). For time values above 10, no difference in the shape of the flowing mass can be seen.

For non-zero inclinations, the convergence towards the similarity solution is slower. As shown in figure 3 for a flume inclination $\theta = 6°$, we have to wait until $t = 256$ for the deviation between the numerical and composite solutions to drop to zero. Note however that for $t \geqslant 32$ the front position given by the composite solution (2.27) slightly deviates from the front computed numerically by less than 5 % and the shapes are very close. Indeed, as shown in figure 4, the similarity solution closely approximates the numerical solution at sufficiently long times, i.e. for $t \geqslant 32$.

3. Slope-dominated regime

We now use perturbation methods and matched asymptotic expansions to study the behaviour of the Newtonian fluid released down a sloping bed, whose inclination

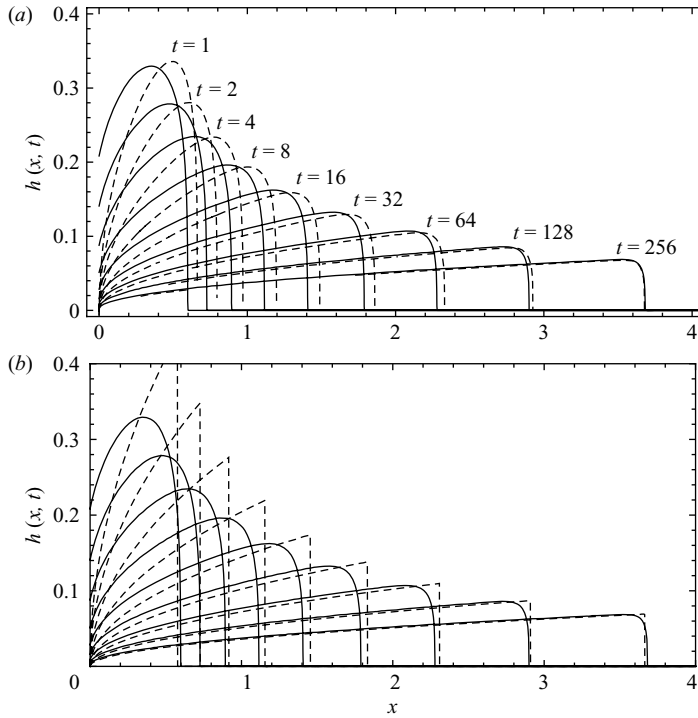† Lister (1992) gave certain details on how to find the inner solution, but did not provide a complete solution.

FIGURE 3. Flow-depth profiles provided by numerical equation (solid line) of the nonlinear diffusion equation for $\theta = 6°$ at dimensionless times $t = 1, 2, 4, 8, 16, 32, 64, 128$ and 256. In subplot (a), we plotted the analytical approximation (2.27) obtained by composing the inner and outer similarity solutions (dashed line). In subplot (b), the analytical solution (3.7) corresponding to pure convection is reported. Computations were made with $\kappa = 0.186$.
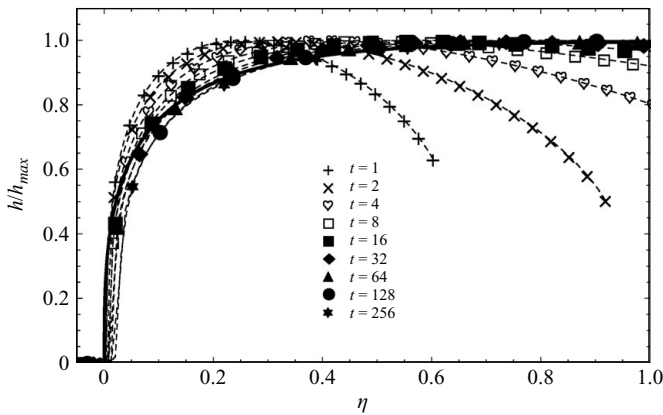

FIGURE 4. Flow-depth profiles $h(\eta, t)/t^{-1/5}$ normalized by $h_{max} = \sqrt{\xi_f/3}$: we plotted our numerical simulations (thin dashed lines marked with symbols) and composite solutions (thick line) obtained by taking the $t \to \infty$ limit of (2.27) for $\theta = 6°$ at dimensionless times $t = 1, 2, 4, 8, 16, 32, 64, 128$ and 256. Computations were made with $\kappa = 0.186$.

may be large. As sketched in figure 1, the flow can be split into two different regions: the body and the front, where the flow depth drops to zero. For the body, the leading-order terms of the governing equations are obtained by removing the contributions that depend on ϵ in (2.3) and (2.4) while keeping Re order one. As readily seen in

the momentum equations, the bulk of the flow is in a nearly steady regime, where gravity acceleration is counterbalanced by the cross-stream gradient of the shear stress. Since this behaviour conflicts with the boundary condition (2.9), a boundary layer correction is needed at the front. Indeed, the steady-regime solution is no longer valid within the tip region because the pressure gradient $\epsilon \partial_x p$ becomes non-negligible. The dynamics of the front is then controlled by the balance between the streamwise pressure and stress gradients, $\epsilon \partial_x p \sim \epsilon h/\xi$ and $\partial_y \sigma_{xy} \sim (u/h)/h$, respectively,

$$\epsilon \frac{h}{\xi} \sim \frac{(u/h)}{h}, \tag{3.1}$$

with $\xi = x - x_f$ and $u \propto h^2$. The extent of the boundary layer can then be estimated as $\xi = O(\epsilon h)$. In this subsection, we will describe the solution for the body, referred to as the *outer solution*, while in the next subsection, attention will be focused on the boundary layer correction (called *the inner solution*). The inner solution smoothly connects to the outer solution at $x = x_f$ for the flow depth. For the velocity field, a more refined matching procedure is required, in which an intermediate expansion must be considered to patch the inner and outer solutions; this situation is also encountered in some capillary-driven flows (Hocking & Rivers 1982; Cox 1986).

3.1. *Body behaviour*

We pose the following asymptotic expansions for the velocity, pressure and flow depth: $u = u_0 + \epsilon u_1 + \cdots$, $p = p_0 + \epsilon p_1 + \cdots$ and $v = v_0 + \epsilon v_1 + \cdots$. Taking $Re = O(1)$ and $Ca \gg 1$ and keeping terms of order zero in the governing equations (2.2)–(2.4), we transform the Navier–Stokes equations to obtain the following set of equations:

$$3 + \frac{\partial^2 u_0}{\partial y^2} = 0, \tag{3.2}$$

$$1 + \frac{\partial p_0}{\partial y} = 0, \tag{3.3}$$

with the same boundary conditions as previous for the diffusive–convective regime. The pressure is still hydrostatic to leading order: $p_0 = h_0 - x$. Integrating (2.12) twice provides the flow-depth averaged velocity: $\bar{u}_0 = h_0^2$. We end up with a nonlinear convection equation that governs the flow-depth variation with time

$$\frac{\partial h_0}{\partial t} + \frac{\partial h_0^3}{\partial x} = 0. \tag{3.4}$$

This equation is similar to the governing equation of h for the body of a viscous sheet in a diffusive–convective regime at long times. As previously, we can solve the governing equation by seeking similarity solutions, but a full analytical solution to the boundary initial value problem can be worked out by using the method of characteristics. The governing equation (3.4) can be recast into the characteristic form

$$\frac{dh}{d\tau} = 0 \quad \text{with} \quad \frac{\partial t}{\partial \tau} = 1 \quad \text{and} \quad \frac{\partial x}{\partial \tau} = 3h^2, \tag{3.5}$$

where τ is a dummy variable. The convection equation being hyperbolic, discontinuities can develop and propagate at a velocity $\dot{s}$ given by

$$\dot{s} [\![h]\!] = [\![h^3]\!], \tag{3.6}$$

where $[\![h]\!]$ is the jump experienced by h across the shock located at $x = s(t)$. Taking the initial conditions $t(0) = 0$, $x(0) = x_0$ and $h(0) = h_i(x_0)$ given by (2.10) into account
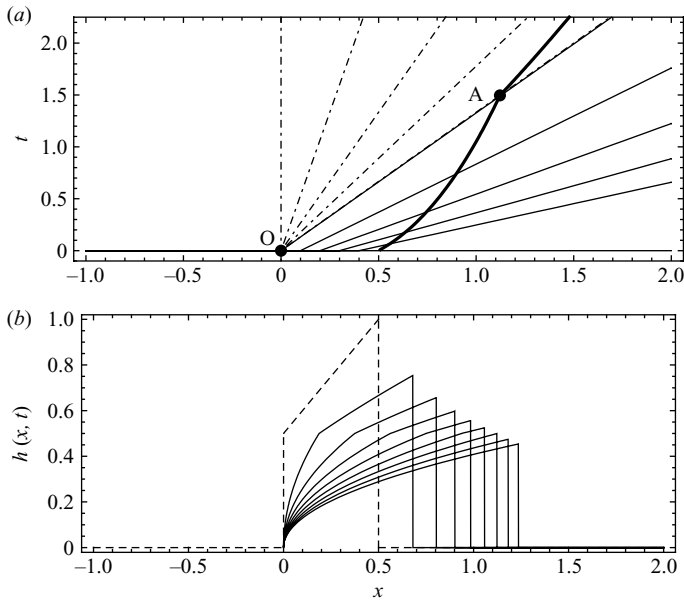
FIGURE 5. (*a*) Characteristics of the convection equation (3.4) in the *x*–*t* plane. The thin solid lines represent the characteristics emanating from $x = 0$ with a slope imposed by the initial flow-depth profile. The dot-dashed lines are the characteristic fan originating from the point of origin O and representing the rarefaction wave at the tail of the flowing mass. The thick line is the locus of the front position $x = s(t)$; at point A, the steepest characteristic $x = m_0 t$ emanating from O intersects the shock curve, which produces a kink in the shock curve. (*b*) Evolution of $h(x, t)$ from $t = 0$ (dashed line) to 2 by 0.25 time step (solid lines); for $t > t_A = 1.49$, the profiles become parabolic. Computations made for $\kappa = 1/2$.

and eliminating τ, we find that

$$h(x, t) = \frac{\sqrt{12\kappa t(\kappa(x - \ell) + h_g) + 1} - 1}{6\kappa t}. \tag{3.7}$$

Initially, at $x = 0$ and $x = \kappa$, the flow depth discontinuously drops to 0. At the right end of the reservoir, this initial discontinuity gives rise to a shock, which propagates at the velocity $\dot{s}$ prescribed by (3.6): $\dot{s} = h_f^2$, where h_f denotes the flow depth at the front and is evaluated using (3.7) at $x = s$. At the left end of the reservoir, a centred rarefaction wave propagates into the tail of the flowing mass (see figure 5). Its features are deduced by seeking wave solutions in the form $\mathcal{H}(\zeta)$ to the convection equation (3.4), with $\zeta = x/t$ (Courant & Friedrich 1948). We find that

$$\mathcal{H}(\zeta) = \sqrt{\tfrac{1}{3}\zeta}. \tag{3.8}$$

The characteristics associated with this rarefaction wave form a fan of straight lines emanating from the point of origin $(x, t) = (0, 0)$: $x = mt$, with m a parameter satisfying $0 \leqslant m \leqslant m_0$ and $m_0 = 3(h_g - \kappa\ell)^2$ (as shown in figure 5*a*). At time t_A, the steepest characteristic coming from O intersects the frontal shock curve $x = s(t)$ at point A. For time $t \leqslant t_A$, the flow-depth profile is piecewise continuous with $h(x, t)$ given by (3.7) for $m_0 t \leqslant x \leqslant s(t)$ and by (3.8) for $0 \leqslant x \leqslant m_0 t$. Time t_A is the time at which the flow depth becomes independent of the initial conditions and conforms to a parabolic shape given by (3.8) (as shown in figure 5*b*).

3.2. *Behaviour within the tip region*

As shown in the previous subsection, there is a boundary layer of size ϵ at the front. To see what is occurring in this boundary layer, we make the following change of variable:

$$x' = \frac{x - x_f(t)}{\epsilon}.$$

In the mobile frame attached to the front, the dominant balance in the momentum balance equation (2.3) is between the streamwise gradient of the pressure and the cross-stream gradient of the shear stress, suggesting that the proper velocity scale is now $U_{diff} = \epsilon^{3/2} U_*$ (like in the purely diffusive regime, with a corrective term to account for slope effect). The flow depth must then scale as $h = O(\epsilon)$ so that the streamwise gradient of the pressure balances the cross-stream gradient of the shear stress provided that $S = \cot\theta\epsilon^{1/2} = O(1)$; we then pose

$$\epsilon = \tan^2\theta. \qquad (3.9)$$

Setting $S = 1$ is arbitrary, but entails no loss of generality. We now embody this scaling analysis into an asymptotic analysis by substituting the following stretched variables into the governing equations (2.3)–(2.4): $x = x_f + \epsilon x'$, $y = \epsilon y'$, $t = \epsilon t'$, $u = \epsilon^{3/2} u' = \epsilon^{3/2} u'_0 + \cdots$, $v = \epsilon^{3/2} v' = \epsilon^{3/2} v'_0 + \cdots$, $h = \epsilon h'_0 + \cdots$ and $p = \epsilon p'_0 + \cdots$.

The re-scaled momentum balance equations are

$$\epsilon^{1/2} Re\left(\frac{\mathrm{d}u}{\mathrm{d}t'} - \dot{x}_f \frac{\partial u}{\partial x'}\right) = 3\epsilon^{1/2} - 3S\frac{\partial p}{\partial x'} + \epsilon^2 \frac{\partial^2 u'}{\partial x'^2} + \frac{\partial^2 u'}{\partial y'^2}, \qquad (3.10)$$

$$\epsilon^{3/2} Re\left(\frac{\mathrm{d}v}{\mathrm{d}t'} - \dot{x}_f \frac{\partial v}{\partial x'}\right) = -3\cot\theta\left(1 + \frac{\partial p}{\partial y}\right) + \epsilon^{5/2}\frac{\partial^2 v'}{\partial x'^2} + \epsilon^{1/2}\frac{\partial^2 v'}{\partial y'^2}. \qquad (3.11)$$

The stress boundary conditions at the free surface $y = h(x, t)$ imply that $p' = 0$ and $\partial y' u' = 0$. The matching conditions also demand that the velocity fields and flow depth smoothly connect to the outer solution for $x' \to -\infty$; among others, we have

$$\lim_{x' \to -\infty} h(x', t') = h_f, \qquad (3.12)$$

with h_f the flow depth at $x = x_f$ given by the outer solution. Keeping Re order one and dropping all terms of order one or higher, we can integrate the momentum balance equations (3.10) and (3.11) to obtain

$$p_0 = h_0 - y \quad \text{and} \quad u'_0 = -\tfrac{3}{2} S \partial_{x'} h'_0 (2h'_0 - y') y'. \qquad (3.13)$$

Note that the velocity field given above does not patch with the outer solution, which imposes $u' \propto 3\left(h' - (1/2)y'\right) y'$ in the $x' \to -\infty$ limit. To cure this, we must introduce an intermediate variable $x = \epsilon^{1/2} x''$ as well as $y = \epsilon^{1/4} y''$, $u = \epsilon^{1/2} u''$, $h = \epsilon^{1/4} h''$ and $p = \epsilon^{1/4} p''$. This produces a velocity profile $u'' = 3(1 - \cot\theta \partial_{x''} h_0)(2h''_0 - y'')y''/2$, which smoothly connects to the inner and outer solutions in the $x'' \to 0$ and $x'' \to -\infty$ limits, respectively. This transition zone is rather thin and can be neglected here.

Integrating the velocity profile (3.13) leads to the flow-depth averaged velocity $\bar{u}' = -S\partial_{x'} h h'^2$ or equivalently $\bar{u} = -S\epsilon^{-1/2}\partial_{x'} h h^2 = -\cot\theta \partial_{x'} h h^2$ to leading order. The evolution equation for the flow depth is then

$$\frac{\partial h}{\partial t'} + \frac{\partial}{\partial x'} G(h) = 0, \quad \text{with} \quad G(h) = -h^3 \cot\theta \frac{\partial h}{\partial x'} \qquad (3.14)$$

and subject to the boundary condition (3.12). Since the volume of fluid contained in the inner region is order ϵ, mass is merely redistributed with no creation or loss

within the head. The initial condition for the evolution equation (3.14) is

$$\left.\begin{array}{ll} h(x', 0) = h_f & \text{for } x' \leqslant 0, \\ h(x', 0) = 0 & \text{for } x' > 0. \end{array}\right\}. \tag{3.15}$$

The initial boundary value problem (3.14) and (3.15) must be solved numerically. For this purpose we used the *pdepe* routine provided in Matlab to solve parabolic differential equations in one space variable. Note that (3.14) also admits asymptotic solutions as seen in §2.2.

After substituting the stretched variables (x', t') with the original scaled variables $(x = x_f + \epsilon x', t = \epsilon t')$ in the solution to (3.14), we obtain a composite solution made up of the outer solution h_{outer} and the inner solution h_{inner}

$$h_{comp.} = h_{outer} + h_{inner} - h_{front}, \tag{3.16}$$

where $h_{front} = h_f$ is their overlap value (i.e. the flow depth at the front of the outer solution), h_{outer} the solution to (3.4) and h_{inner} the solution to (3.14). The composite solution provides a uniform approximation of the solution to leading order.

3.3. *Remarks and summary*

Except for the aspect-ratio number ϵ, the inner and outer solutions for the slope-dominated regime have the same behaviour as the solutions related to the diffusive–convective regime: at fairly short times after the slumping phase, the body (outer solution) is in a convective regime close to a steady-uniform flow, while the head dynamics is dominated by the balance between pressure gradient and viscous dissipation. Physically, there is not much difference between the diffusive–convective and slope-dominated regimes and thus no real transition from one to another one. In particular, the long-term approximation for the flow-depth profile pertaining to the body (outer solution) is the same for both regimes [see (2.20) and (3.8)], while the head has nearly the same shape. Taking a closer look at the outer solution worked out in §3.1 unveils some interesting features: to solve the initial boundary value problem, we had to solve a double Riemann problem at the left and right ends of the initial volume. The left-end discontinuity gives rise to a rarefaction wave, which quickly overtakes the shock wave issuing from the right end. As shown in figure 5 on a particular example, the rarefaction wave catches up the shock wave at the end of the slumping phase, after the front travelled a distance ℓ; the details of the initial conditions dissipate rapidly, which explains why the similarity solution provides a fairly good representation of behaviour although the initial volume is considered a point source. This also shows that although the flow is in a subcritical regime (with a Froude number lower than 0.1) for which both upstream and downstream boundary conditions are expected to play a role, its dynamics is entirely controlled by the rarefaction wave emanating from the tail; the head is pushed forward by the body and must then accommodate change imposed by the latter.

4. Experiments

4.1. *Experimental facility*

We used a 30 cm wide, 4 m long flume fed by a reservoir, as sketched in figure 1. The flume laid on an aluminium plate, which was 4 m long, 1.8 m wide and could be inclined from $0°$ to $45°$. Its position was accurately controlled using a digital clinometer with a precision of $0.1°$. The plate was supported by a frame made of profiled aluminium beams to ensure rigidity.
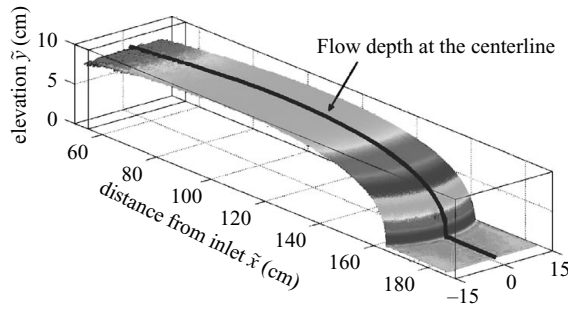
FIGURE 6. Reconstruction of the free surface using image processing for slope $\theta = 12°$ and time $t = 28$ s (after Cochard 2007).

The reservoir was positioned at the top of the inclined plane behind the dam wall. The maximum capacity of the reservoir was 120 kg. The dam wall was composed of a 1.6×0.8 m^2 ultralight carbon plate. Two pneumatic jacks opened the sluice gate at the desired aperture within 0.5 s. An ultralight dam wall was needed to reduce dam-wall inertia, plane vibration and jerk. The two jacks were quickly raised by injecting air pressured at 7 MPa. Two electromagnetic sensors were located at the tip of each jack to control its position and reset the clock.

Before each run, the fluid was gently poured into the reservoir, while the inclined plane was kept in the horizontal position. The flume was then inclined at a given slope. The material was then left at rest until its free surface became horizontal. At time $t = 0$, the sluice gate was raised and the material started accelerating and flowing. The surge motion was imaged by a digital camera. When the front went beyond the imaged area, we stopped recording images. The material was then removed from the flume and the plane was carefully cleaned out.

To accurately measure the surge's free-surface variations with time, we have developed a new imaging system, consisting of a digital camera (Basler A202k Pixels camera provided by Qualimatest, Geneva, Switzerland) coupled with a synchronized micromirror projector (modified z-Snapper provided by ViaLux, Chemnitz, Germany). The object's surface was imaged into a camera and patterns were projected onto the surface under an angle of incidence that differed from the imaging direction (Cochard 2007; Cochard & Ancey 2008). From the deformed pattern recorded by the camera, the phase could be extracted and, using unwrapping algorithms, the height was computed and the free surface reconstructed. We were able to measure the free surface of the flow to within 1 mm every 22 ms.

As shown in figure 6, we measured the flow-depth profile at the centreline of the flow. To attenuate noise effects, the flow depth was averaged over at 10 pixel band along the centreline (approximately 1 cm). Note also in this figure that the contact line was a flattened parabola, whose shape was nearly independent of time (except at early times during the slumping phase) and since we worked at high capillary numbers, the contact line was stable. The position of the front was evaluated at the flow centreline seeking the position at which the flow thickness dropped below a given threshold. On some occasions, locating the front accurately was difficult because of glints arising at the free surface near the contact line; these glints blurred the projected patterns and introduced noise in the post-treatment phase. The uncertainty on the front position could then be as high as 5 mm.

θ (deg.)	Mass (kg)	$\tilde{h}_g$ (cm)	μ (Pa s)	Re	Ca	L_* (m)	H_* (cm)	T_* (s)
0	56.1	25.8	345	10^{-3} to 0.05	15–261	1.18	10	131
6	56.7	28.8	352	6×10^{-3} to 0.13	81–671	3.47	3.8	1712
12	57.0	31.6	352	11×10^{-3} to 0.35	161–1606	1.72	7.7	104
18	57.6	34.8	345	17×10^{-3} to 0.72	239–2895	1.13	11.9	19.1
24	50.8	34.7	345	23×10^{-3} to 0.94	315–378	0.77	15.3	5.99

TABLE 1. Features of each experimental run: for each slope θ, the mass of glucose contained in the reservoir, the maximum gate aperture $\tilde{h}_g$ and the viscosity μ measured at room temperature are reported. The typical range of variation of the Reynolds and capillary numbers Re and Ca, respectively, are also indicated. We also report the length, flow depth and time scales $L_* = \sqrt{V/\epsilon}$, $H_* = \sqrt{V\epsilon}$ and T_*, respectively.

4.2. Material

Highly concentrated glucose–water solutions were used. Compared to industrial oils, glucose syrup offers many advantages: it is a non-toxic product that is easy to clean out of the flume (using hot water) and is relatively inexpensive. It can be coloured in white using titanium dioxide, which is essential to enhancing contrast for image processing. Depending on the glucose concentration in the solution, the dynamic viscosity ranges from 10^{-3} to 10^4 Pa s. There are, however, some disadvantages that make its use somewhat delicate. At high concentrations, glucose syrup is unstable and crystallizes rather quickly, in particular when impurities (e.g. titanium dioxide) are added to the solution. In practice, once prepared, the solution must be used within 2 days. To reach high glucose concentrations, one must heat the solution at temperatures as high as $110\,°C$, but because of Maillard's reaction, the syrup may blacken, which is a major impediment for image contrast.

In practice, we prepared large volumes of glucose by melting 75 kg of dextrose monohydrate (in three 25 kg batches). While vigorously mixing the solution on a regular basis, we maintained it in an oven at a temperature of $130\,°C$ until it was fully liquid and homogeneous (i.e. with no crystals). The solvent was deionized water, which was progressively added such that the final mass solution concentration was 95.8%, which allowed us to reach viscosities close to 350 Pa s at $20\,°C$ (Schenck 2007). A small quantity of titanium oxide (50 g) was also added to whiten the syrup. The solution was then cooled to $20\,°C$ as quickly as possible to avoid crystallization. A mass of approximately 50 kg was then gently poured into the reservoir. A fluid sample was collected and its rheological behaviour was characterized using a Bohlin CVOR rheometer and cone-and-plate geometry. All runs were carried out in a room at constant temperature and hygrometry.

Table 1 summarizes the value of the parameters for each experimental run. The surface tension was $\gamma = 0.06$ Pa m and the density was $\rho = 1420$ kg m^{-3}. In table 1, the range of variation of the Reynolds and capillary numbers is also reported. Initially the aspect-ratio number h_f/x_f ranged from 0.5 ($\theta = 0°$) to 0.68 ($\theta = 24°$), but rapidly dropped below 0.1. On average, the Reynolds number was close to 10^{-2}, while the capillary number was of the order of 200.

4.3. Results for a horizontal flume

Figure 7(a) reports flow-depth profiles at physical times $\tilde{t} = 2^k$ s with $k = 0, 1, \ldots, 8$, i.e. dimensionless times $t = 0.0076 \times 2^k$. We also plotted the similarity solutions (2.18). The shape of the flowing mass is correctly predicted, but taking a closer look at
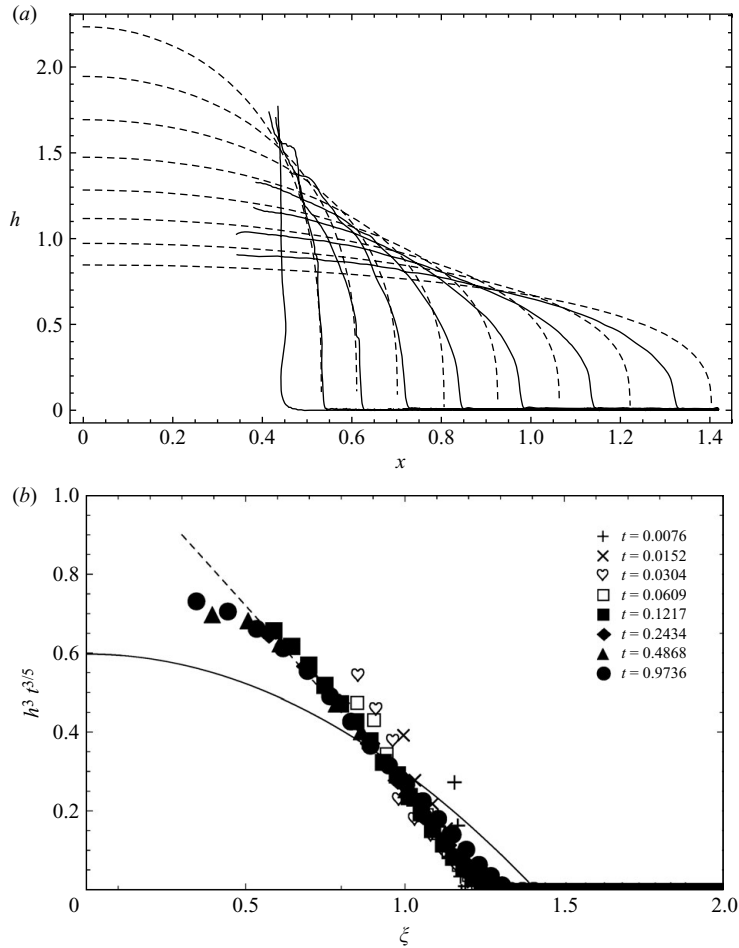
FIGURE 7. (a) Flow-depth profiles $h(x, t)$: experimental data (solid lines) and similarity solutions (dashed lines) at times $t = 7.6 \times 10^{-3}$, 15.2×10^{-3}, 30.4×10^{-3}, 60.8×10^{-3}, 0.122, 0.243, 0.486 and 0.973. (b) Flow-depth profile $(h/t^{-1/5})^3$ as a function of $\xi = x/t^{1/5}$: experimental data and similarity form (solid line) given by (2.18) are reported; the dashed line $(h/t^{-1/5})^3 = (9/10)(1.3 - \xi)$ is the best-fit line.

figure 7(b), where we scaled the data by plotting $(h/t^{-1/5})^3$ as a function of $\xi = x/t^{1/5}$, shows that the data collapse onto a single curve, but this curve differs slightly from the expected similarity form. The experimental curve $(h/t^{-1/5})^3$ has a finite slope that matches the theoretical value at the leading edge, but there seems to be a systematic shift between the two curves: the theoretical curves are ahead of $\Delta\xi = 0.15$. This phenomenon is even clearer when plotting the front position as a function of time (see figure 8). At short times, we observed that the front hardly moved, then for times greater than 5×10^{-3}, it accelerated more frankly. This slumping phase is not properly described by the similarity solution, which is normal since it describes how the flowing mass behaves after a certain period of time when the initial conditions no longer influences flow dynamics. At longer times, the experimental curve parallels the theoretical curve for the range of experimental times 10^{-2} to 1. There is little evidence that it would have converged towards the theoretical curve just after the maximum observation time.
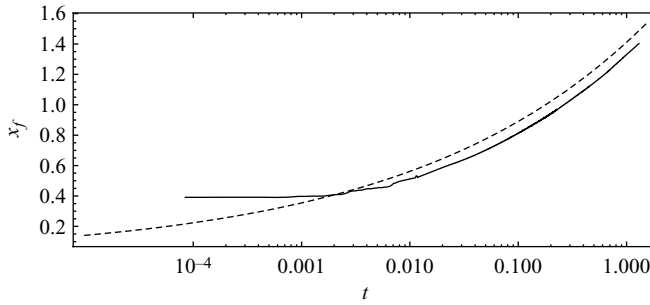
FIGURE 8. Front position with time for $\theta = 0°$ in a log-linear plot: experimental data (solid line) versus theoretical curve (dashed line) $x_f = \xi_f t^{1/5}$ with ξ_f given by (2.19).

Returning to figure 7(*b*), we also observe that far away from the contact line, the experimental profile $(h/t^{-1/5})^3$ varies nearly linearly with ξ, while the similarity solution predicts a profile varying as $\xi_f^2 - \xi^2$. In summary, the $t^{1/5}$ scaling for the front position is in agreement with experiments, but there is a systematic shift with the experimental data. The normalized flow-depth profiles $(h/t^{-1/5})^3$ approach a similarity form closer to $9/10(1.3 - \xi)$ than $3/10(\xi_f^2 - \xi^2)$.

This systematic shift between experimental and theoretical curves may result from the initial conditions. Indeed, when the gate was opened, a fluid layer of approximate thickness $\sqrt{\mu \Delta t_\ell / \rho} = 0.3$ m (with $\Delta t_\ell \sim 0.5$ s the typical time needed to open the gate) was lifted up with the plate. This uplift of the fluid was sufficient to cause delay and may partly explain why the experimental curve deviates from the theoretical curve. As shown with numerical simulations, when the flume inclination is zero, the asymptotic solution is approached at long times (typically longer than 200); at short times, the similarity solution was significantly ahead of the numerical solution (see figure 3). Another explanation lies in the three-dimensional nature of the flows in our flume. Because of sidewalls, there was a shear gradient in the cross-stream direction. A crude analysis shows that the ratio R of the downstream-to-cross-stream shear stresses is of the order of W/h, with W the flume width. Here, typically at $\tilde{t} = 120$ s, we had $h \sim 4$ cm, which yields $R \sim 7$, showing that even at late times, the flow structure remained three-dimensional. This may explain why the front was late relative to the theoretical solution, but this does not explain why the flow-depth profile far away from the contact line deviates from the similarity form. Indeed, since the flow-depth profile was measured at the centreline, the cross-stream shear rate was virtually zero and the flow structure was expected to be two-dimensional there.

4.4. *Results for sloping flumes*

Theoretically, we expect the front $x_f = \xi_f t^{1/3}$ with ξ_f given by (2.21), which implies that $(x_f/\xi_f)^3$ varies linearly with time. Figure 9 shows that for flume inclinations ranging from 6° to 24°, this ratio effectively tends towards a straight line at sufficiently long times, but this experimental trend parallels the theoretical curve $(x/\xi_f)^3 = t$ (solid line) without converging towards it. Again, we find a systematic shift between the experimental and theoretical curves. On the same figure, we have plotted the front position $x_f + \epsilon x'_f$ for the composite solution (3.16) computed for each plane inclination (dashed lines). The curves converge towards the similarity solution at sufficiently long times. While they provide a reasonable approximation of the observed behaviour at short times, they parallel the experimental trend at long times without tending
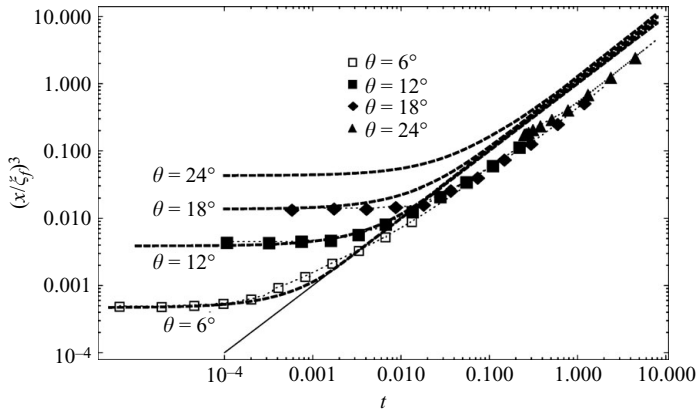
FIGURE 9. Normalized front position $(x_f/\xi_f)^3$ as a function of time in a log–log representation: the experimental curves (dotted line marked with symbols) related to $\theta = 6°$, $12°$, $18°$ and $24°$ slopes are indicated. The solid line represents the theoretical curve $(x/\xi_f)^3 = t$ corresponding to the outer similarity solution (2.21). The thick dashed lines stand for the front position $x_f + \epsilon x'_f$ for the composite solution (3.16) computed for each slope.

towards them. We do not report here flow-depth profiles since they present the same type of information as figure 7(*a*) if we remain at a qualitative level. The systematic delay between the experimentally observed and computed front positions makes it difficult to test the model reliability by merely looking at the evolution of $h(x, t)$ profiles. To further expand our analysis we need to replot the flow-depth profiles as functions of $\eta - \eta_f$ or $x_f - x$ to compare the experimental data with the curves provided by the composite solutions (2.27) and (3.16) at different times.

We first address the occurrence of a diffusive–convective regime, for which ϵ was order $\tan\theta$. Figure 10 shows the normalized flow-depth profiles $h(\eta, t)/h_{max}$ as a function of the inner variable $\eta - \eta_f$ for slopes in the $6°$–$24°$ range, where h_{max} is the maximum thickness of the viscous sheet at time t and $\eta = (\xi_f - \xi)t^{2/3}$ (with $\xi = x/t^{1/3}$). As seen by comparing the different subplots, there is a contrasted effect of slope on the experimental curves. For $\theta = 6°$, the experimental data at sufficiently long times ($t > 0.1$) collapse onto a single line, which does not differ too much from the theoretical curves computed at the same times. For $\theta = 12°$, the data come close to the master curve (dashed line) obtained by taking the $t \to \infty$ limit of the composite solution (2.27), but do not fall on the composite-solution curve when the latter is computed at the same time as the data; this is in line with the systematic delay observed for the front position. For both slopes, the nose presents a very steep face. At higher slope values ($\theta \geqslant 18°$), the tip region presents an acuter angle and data are clearly below the theoretical profile (regardless of the time at which the solution is computed). The deviation from the theoretical curve at higher slopes is expected since the theoretical developments hold for $\epsilon = \tan\theta \ll 1$.

We then address the slope-dominated regime, for which ϵ scales as $\tan^2\theta$. Figure 11 shows the normalized flow-depth profiles $h(x, t)/h_{max}$ as a function of the distance to the front $x_f - x$ for slopes θ ranging from $6°$ to $24°$, where h_{max} is the maximum thickness of the viscous sheet at time t. For $\theta = 6°$, theoretical curves significantly deviate from the experimental data (as expected). At higher slopes ($\theta \geqslant 12°$), the experimental data at sufficiently long times ($t > 0.1-0.2$) come close to the theoretical curves, which confirms that the scaling used in §3 is appropriate.

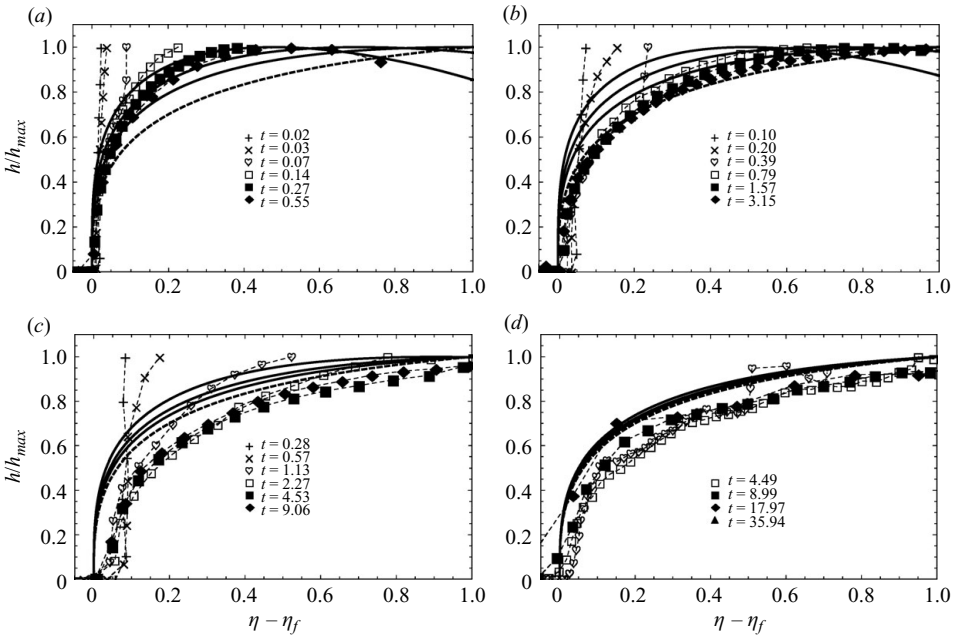FIGURE 10. Flow-depth profiles $h(\eta, t)$ normalized by the maximum flow depth h_{max} when $\epsilon = \tan \theta$ for $\theta = 6°$ (*a*), $\theta = 12°$ (*b*), $\theta = 18°$ (*c*) and $\theta = 24°$ (*d*) at different dimensionless times. Thick solid lines represent the composite solutions (2.27) computed at three different times (the last three times of each series). The dashed line represents the $t \to \infty$ limit of the composite solution (2.27).
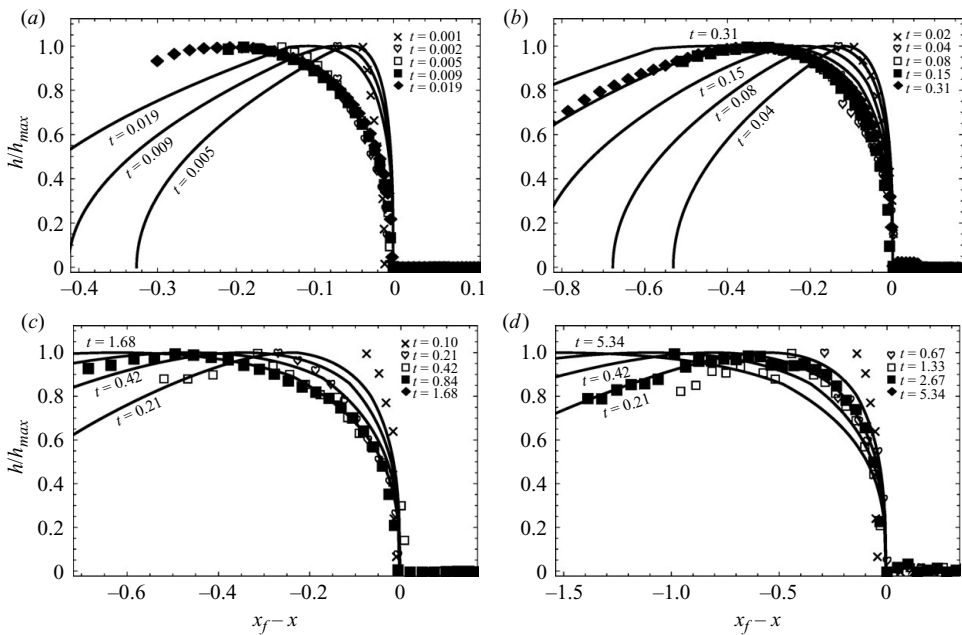

FIGURE 11. Flow-depth profiles $h(\eta, t)$ normalized by the maximum flow depth h_{max} when $\epsilon = \tan^2 \theta$ and for $\theta = 6°$ (*a*), $\theta = 12°$ (*b*), $\theta = 18°$ (*c*) and $\theta = 24°$ (*d*) at different dimensionless times. We also plotted the composite solutions (thick line) by computing (3.16) at three different times (reported above each curve).

5. Concluding remarks

In this paper, we investigated the dam-break problem, where a fixed large volume of glucose was unleashed into a flume. Theoretically, we idealized this setting as a two-dimensional problem. When slope was shallow, we used lubrication theory and followed earlier authors (Huppert 1982*a*,*b*; Grundy 1983*a*; Gratton & Minotti 1990; Lister 1992; Witelski & Bernoff 1998; Mathunjwa & Hogg 2006) by seeking similarity solutions to the Navier–Stokes equations in the low-Reynolds-number and high-capillary-number limit. Slope shallowness implies that the aspect ratio ϵ must be order $\tan\theta$. This scaling no longer holds at large slopes. In that case, we used perturbation techniques and matched asymptotic expansions to find analytical approximate solutions to the initial boundary value problem; we also found that ϵ must scale like $\tan^2\theta$.

In recent years, much attention was paid to shallow slopes, for which similarity solutions can be worked out (our paper just summarized the early work). These solutions represent the intermediate asymptotics, i.e. they describe the behaviour of the flowing mass of fluid after a certain length of time when the initial conditions have been forgotten. It is now well accepted that similarity theory is an indispensable tool not only to provide analytic solutions to the equations of motion, but also to shed light on the physical behaviour of a system at sufficiently long times, i.e. after the details of the initial conditions have dissipated (Barenblatt 1996). A critical point for the meaningfulness of similarity solutions lies in the convergence rate towards a similarity form, that is, the time needed for the solution to any initial value problem to approach the similarity form. The only initial parameter that matters for the similarity solutions is the volume of fluid released, which is needed to compute the spreading rate. We first investigated the dam-break problem for shallow slopes numerically, then experimentally.

Numerically, we found that the solution to our initial value problem converged rather quickly towards the similarity form when the flume inclination was zero. In contrast, it took much more time for the initial-value solution to approach the similarity form for non-zero flume inclinations. Typically, we found that for physical times of the order $\tilde{t} \sim 24\mu\ell^2/(\rho g \tilde{h}_g^3)$, the differences between numerical and similarity solutions did not exceed 1 % when the flume inclination was zero, whereas for a slope of 6°, it was not until $\tilde{t} \sim 768\mu/(\rho g \cos\theta \tilde{h}_g)$ that convergence was observed. This difference in the convergence rate reflects the difference in the governing processes. For zero inclinations, the governing process is diffusion. In this case, the initial discontinuity in the volume shape was rapidly smoothed out when the fluid slumped. For non-zero inclinations, the body behaviour of the flowing mass is controlled by convection, while the behaviour in the leading edge is dominated by a balance between the temporal evolution of h and diffusion. The thickness of the frontal boundary layer accounted for approximately 20 % of the flow thickness and thus decreased with time, giving the nose the appearance of a shock wave in the course of motion.

Experimentally, the data collected in the flume tell a slightly different story. For horizontal and sloping flumes, we observed that the front position scaled as $t^{1/5}$ and $t^{1/3}$, respectively, as expected using similarity theory. There was, however, a systematic delay between the observed and computed front positions. This delay may be explained by the uplift of part of the fluid caused by removing the gate and the three-dimensional nature of the flows (induced by the finite width of the flume). Another troublesome aspect was the flow-depth profiles. The experimental profiles exhibited similarity properties, but the similarity shape differed from the theoretical

shape. For zero flume inclination, the flow depth at the contact line was properly described by theory, but as one goes away from the front, the flow-depth profile varies: $(x_f - x)^{1/3}$ rather than $(x_f^2 - x^2)^{1/3}$. For sloping flumes, we observed that for mild slopes (θ in the $6°$–$12°$ range) the experimental profiles came close to the theoretical profile given by the inner similarity solution.

For large slopes ($\theta > 12°$), a different scaling is required for ϵ: ϵ scales as $\tan^2\theta$ rather than $\tan\theta$. Except for the systematic delay between the computed and observed front positions, good agreement is found between theory and experiment for the flow-depth profiles. In spite of a few differences in the mathematical treatment, the governing equations and solutions at large and shallow slopes are very similar. At fairly short times after the slumping phase, the body (outer solution) is in a convective regime close to a steady-uniform flow, while head dynamics is dominated by the balance between pressure gradient and viscous dissipation. The long-time approximation for the outer solution (body) is the same for both slope ranges [see (2.20) and (3.8)]. Examination of the outer solution worked out in §3.1 shows that the details of the initial conditions dissipate rapidly, which explains why the similarity solution provides a fairly good representation of behaviour. Another striking point is that although the flow is in a subcritical regime (with a Froude number in the 0.001–0.1 range), its dynamics is entirely controlled by the rarefaction wave emanating from the tail; the head is pushed forward by the body and accommodates change imposed by the latter.

REFERENCES

BARENBLATT, G. I. 1996 *Scaling, Self-Similarity, and Intermediate Asymptotics*. Cambridge University Press.

BUCKMASTER, J. 1977 Viscous sheets advancing over dry beds. *J. Fluid Mech.* **81**, 735–756.

COCHARD, S. 2007 Measurements of time-dependent free-surface viscoplastic flows down steep slopes. PhD thesis, Ecole Polytechnique Fédérale de Lausanne.

COCHARD, S. & ANCEY, C. 2008 Tracking the free surface of time-dependent flows: image processing for the dam-break problem. *Exp. Fluids* **44**, 59–71.

COURANT, R. & FRIEDRICH, K. O. 1948 *Supersonic Flow and Shock Waves*. Intersciences Publishers.

COX, R. G. 1986 The dynamics of the spreading of liquids on a solid surface. Part 1. Viscous flow. *J. Fluid Mech.* **168**, 169–194.

DIDDEN, N. & MAXWORTHY, T. 1982 The viscous spreading of plane and axisymmetric gravity currents. *J. Fluid Mech.* **121**, 27–42.

DIEZ, J. A., GRATTON, R. & GRATTON, J. 1992 Self-similar solution of the second kind for a convergent viscous gravity current. *Phys. Fluids* A **4**, 1148–1155.

GARABEDIAN, P. R. 1966 Free boundary flows of a viscous liquid. *Comm. Pure Appl. Math.* **19**, 421–434.

GOODWIN, R. & HOMSY, G. M. 1991 Viscous flow down a slope in the vicinity of a contact line. *Phys. Fluids* A **3**, 515–528.

GRATTON, J. & MINOTTI, F. 1990 Self-similar viscous gravity currents: phase-plane formalism. *J. Fluid Mech.* **210**, 155–182.

GRUNDY, R. E. 1983*a* Asymptotic solution of a model non-linear diffusion equation. *IMA J. Appl. Maths* **31**, 121–137.

GRUNDY, R. E. 1983*b* Local similarity solutions for the initial-value problem in non-linear diffusion. *IMA J. Appl. Maths* **31**, 209–214.

GRUNDY, R. E. & MCLAUGHLIN, R. 1982 Large-time solution of a nonlinear diffusion equation. *Proc. R. Soc. London Ser.* A **381**, 395–406.

HOCKING, L. M. 1990 Spreading and instability of a viscous fluid sheet. *J. Fluid Mech.* **211**, 373–392.

HOCKING, L. M. & RIVERS, A. D. 1982 The spreading of a drop by capillary action. *J. Fluid Mech.* **121**, 425–442.

HUNT, B. 1994 Newtonian fluid mechanics treatment of debris flows and avalanches. *J. Hydraul. Engng* **120**, 1350–1363.

HUPPERT, H. E. 1982*a* Flow and instability of a viscous current down a slope. *Nature* **300**, 427–429.

HUPPERT, H. E. 1982*b* The propagation of two-dimensional and axisymetric viscous gravity currents over a rigid horizontal surface. *J. Fluid Mech.* **121**, 43–58.

HUPPERT, H. E. 2006 Gravity currents: a personal perspective. *J. Fluid Mech.* **554**, 299–322.

LISTER, J. R. 1992 Viscous flows down an inclined plane from point and line sources. *J. Fluid Mech.* **242**, 631–653.

MATHUNJWA, J. S. & HOGG, A. J. 2006 Self-similar gravity currents in porous media: linear stability of the Barrenblatt–Pattle solution revisited. *Eur. J. Mech.* B **25**, 360–378.

MAXWORTHY, T. 1983 Gravity currents with variable inflow. *J. Fluid Mech.* **128**, 247–257.

MEI, C. C. 1966 Nonlinear gravity waves in a thin sheet of viscous fluid. *J. Maths. Phys.* **45**, 266–288.

NAKAYA, C. 1974 Spread of fluid drops along a horizontal plane. *J. Phys. Soc. Jpn.* **37**, 539–543.

NSOM, B. 2002 Horizontal viscous dam-break flow: experiments and theory. *J. Hydraul. Engng* **128**, 543–546.

NSOM, B., DEBIANE, K. & PIAU, J.-M. 2000 Bed slope effect on the dam break problem. *J. Hydraul. Res.* **38**, 459–464.

OCKENDON, J. R. 1978 Numerical and analytical solutions of moving boundary problems. In *Moving Boundary Problems* (ed. D.G. Wilson, A.D. Solomon & P.T. Boggs). Academic Press.

SCHENCK, F. W. 2007 Glucose and glucose-containing syrups. In *Ullmann's Encyclopedia of Industrial Chemistry* (ed. H.-J. Arpe), vol. A12, pp. 457–475. Wiley-VCH Verlag GmbH.

SIMPSON, J. E. 1997 *Gravity Currents in the Environment and the Laboratory*. Cambridge University Press.

SMITH, H. S. 1969 On initial value problems for the flow in a thin sheet of viscous liquid. *Z. Angew. Math. Mech.* **20**, 556–560.

SMITH, P. C. 1973 A similarity solution for slow viscous flow down an inclined channel. *J. Fluid Mech.* **58**, 275–288.

TAKAGI, D. & HUPPERT, H. E. 2007 The effect of confining boundaries on viscous gravity currents. *J. Fluid Mech.* **577**, 495–505.

VERETENNIKOV, I., INDEIKINA, A. & CHANG, H.-C. 1998 Front dynamics and fingering of a driven contact line. *J. Fluid Mech.* **373**, 81–110.

VAN VROONHOVEN, J. C. W. & KUIJPERS, W. J. J. 1990 A free-boundary problem for viscous fluid flow in injection moulding. *J. Eng. Math.* **24**, 151–165.

WITELSKI, T. P. & BERNOFF, A. J. 1998 Self-similar asymptotics for linear and nonlinear diffusion equations. *Stud. Appl. Math.* **100**, 153–193.